A Model for Solar Polar Jets

E. Pariat[1,2,3], S. K. Antiochos[1], and C. R. DeVore[2]

[1] *Space Weather Laboratory, NASA Goddard Space Flight Center, Greenbelt, MD 20771, USA*

[2] *Naval Research Laboratory, Washington, DC 20375, USA*

[3] *CEOSR, George Mason University, Fairfax, VA 22030, USA*

epariat@ssd5.nrl.navy.mil

ABSTRACT

We propose a model for the jetting activity that is commonly observed in the Sun's corona, especially in the open-field regions of polar coronal holes. Magnetic reconnection is the process driving the jets and a relevant magnetic configuration is the well-known null point and fan separatrix topology. The primary challenge in explaining the observations is that reconnection must occur in a short-duration energetic burst rather than quasi-continuously as is implied by the observations of long-lived structures in coronal holes, such as polar plumes, for example. The key idea underlying our model for jets is that reconnection is forbidden for an axisymmetric null-point topology. Consequently, by imposing a twisting motion that maintains the axisymmetry, magnetic stress can be built up to large levels until an ideal instability breaks the symmetry and leads to an explosive release of energy via reconnection. Using 3D MHD simulations we demonstrate that this mechanism does produce jets with high speed and mass, driven by nonlinear Alfvén waves. We discuss the implications of our results for observations of the solar corona.

Subject headings: Sun: corona—Sun: magnetic fields

1. Introduction

High spatial and temporal resolution observations from space missions such as SOHO and TRACE have shown that the Sun's photosphere is never topologically simple and the corona is never quiet. The photosphere exhibits a constantly evolving, multipolar flux distribution on scales ranging from the "salt-and-pepper" or "magnetic carpet" (e.g. Harvey

1993; Schrijver et al. 1997; Schrijver & Title 2002) to active region complexes. The corona exhibits brightenings and jets on a vast range of scales, including explosive events (Brueckner & Bartoe 1983; Innes et al. 1997; Pérez & Doyle 2000); SOHO/EIT micro-jets (Gurman et al. 1998) and white light polar jets (Wang et al. 1998; Wang & Sheeley 2002); cool jets entwined with the ubiquitous TRACE "moss" (de Pontieu et al. 1999); EUV "blinkers" (Harrison et al. 2003); and spicules/macrospicules (Yamauchi et al. 2004). It has been argued that the multipolarity of the photospheric field is the key to understanding all of this activity including CMEs, and that reconnection between interacting flux systems is the underlying physical process (e.g. Antiochos 1987, 1998; Karpen et al. 1996).

The simplest type of flux system interaction in the solar corona is that between the closed field of a small bipole and a large-scale background open field. This type of topology is ubiquitous on the Sun and has been seen since the earliest Skylab observations as X-ray bright points in coronal holes (e.g. Golub et al. 1974). The best evidence for reconnection in this topology is the discovery of X-ray jets by the Soft X-ray Telescope (SXT) on *Yohkoh* (Tsuneta et al. 1991). Solar X-ray jets are transitory brightenings with apparent collimated motions (Shibata et al. 1992; Shibata & Murdin 2000). Their observational properties have been thoroughly studied with SXT (Shibata et al. 1994; Canfield et al. 1996; Shimojo et al. 1996, 1998; Shimojo & Shibata 2000b). The new X-range observation provided by the X-ray telescope (XRT; Golub et al. 2007) on *Hinode*, is providing new insights in this phenomena (Cirtain et al. 2007; Savcheva et al. 2007; Shimojo et al. 2007). X-ray jets jets can have velocities above 1000 km/s, reach heights of a solar radius or more, and have kinetic energies of order 10^{28} ergs.

These observation strongly suggests that impulsive magnetic reconnection between the closed field of the bipole and the external open field is the driving mechanism for the jets (Shibata et al. 1997; Shimojo & Shibata 2000a). Numerical simulations of jets have been carried out in 2D (Yokoyama & Shibata 1995, 1996; Miyagoshi & Yokoyama 2004; Isobe et al. 2007), 2.5D (Karpen et al. 1998; Archontis et al. 2007) and 3D (Archontis et al. 2005, 2006; Isobe et al. 2006), but the latter have focused primarily on the interaction between closed field structures. Recently, Moreno-Insertis et al. (2008) developed a 3D MHD numerical simulation of an X-ray jet, based on the interaction of a twisted emerging flux tube with the coronal open field. Although their model agrees well with the observed thermal properties of jets, the extended length of the emerging flux tube causes the generation of a jet that has far more translational symmetry than is observed. Their model may not be able to account for the 3D helical structures frequently observed in jets (e.g. Shimojo et al. 1996; Canfield et al. 1996; Wang et al. 1998; Jiang et al. 2007).

There are, at least, two major difficulties in obtaining a high-energy, high-mass jet in

a fully 3D geometry. The difficulty is that whereas 2D flux surfaces can exchange relative positions only by reconnection, 3D field lines are free to move around each other. Consequently, if we consider the motion of a small bipole through an open-field region, it is not clear that sufficient reconnection will occur to account for the large inferred masses of the observed jets.

The second difficulty is the fundamental problem faced by all reconnection models for explosive solar activity: the reconnection must stay "off" until a large amount of free energy has been built up, then stay "on" until a substantial fraction of this energy has been released. The first requirement is especially challenging for the solar corona, because current sheets generally form at the separatrix surface between flux systems as soon as the flux systems begin to interact. Reconnection, of course, acts to destroy any such current sheet. If the flux system interaction is due to flux emergence or photospheric motions, the separatrix current sheets will build on slow photospheric time scales and dissipate via reconnection well before they contain sufficient energy to account for coronal hole jets. For example, in Parker's classic theory for coronal heating (Parker 1983), current sheet formation is postulated to occur readily as a result of slow footpoint stressing, but these sheets lead to a quasi-steady heating rather than a large mass motion. A very similar quasi-steady reconnection has been postulated to account for long-lived coronal hole plumes (e.g. Wang 1998; Wang & Muglach submitted). The challenge, therefore, to obtaining a short-duration jet rather than a long-lived plume is to build up a strong current sheet before inducing reconnection. In the next section we propose a mechanism for achieving this result.

2. A Mechanism for Explosive Reconnection

Figure 1 shows the fundamental magnetic configuration of our model: a vertical dipole embedded in a vertical, uniform background field. This is a typical assumption for jets (e.g. Shibata et al. 1992; Shibata & Murdin 2000) and also the basic magnetic configuration postulated in models for plumes (Wang 1998) and models for solar wind heating and acceleration (Parker 1958; McKenzie et al. 1995). As is well-known, the topology consists of two flux systems separated by a hemispherical separatrix surface, the so-called fan, which contains a magnetic null point (e.g. Lau & Finn 1990; Antiochos 1998; Priest et al. 1994). Note that this is a true null - all three components of the field vanish. Intersecting the fan at the null are two singular field lines, the inner and outer spines. For the axisymmetric configuration of Fig. 1, the null occurs exactly at the apex of the fan, but it should be emphasized that the topology is unchanged even if the system is non-axisymmetric. For example, if the background field has a tilt, thereby breaking the axisymmetry, the fan, spines, and null are

topologically unchanged.

Assume that, as a result of either footpoint motions or flux emergence, stress has been injected into the closed field inside the fan of Fig. 1. Note that since the external field is open, any stress there would simply propagate away with the solar wind. Now let us freeze the photosphere and consider how reconnection would occur in the two-flux system of Fig. 1. The intersection of the fan with the photosphere defines a closed circle on the photosphere that bounds all the positive flux closing across the polarity inversion line and into the negative spot. Any reconnection requires a change in this separatrix curve, but if the system is to remain axisymmetric, the separatrix curve can change only by expanding or contracting. This is not possible, however, because the net flux inside this curve must vanish. As long as the flux at the photosphere remains fixed, the position of the separatrix curve is also fixed, thereby, forbidding any reconnection irrespective of whatever current sheets form in the system. Note that this conclusion holds only for a two-flux system. For an axisymmetric four-flux topology, which must have multiple separatrix curves on the photosphere, reconnection occurs readily (e.g. Antiochos & Devore 1999; MacNeice et al. 2004).

The result that reconnection is forbidden in an axisymmetric null point topology is a central idea underlying our model for coronal jets. We conjecture that if the topology of Fig. 1 is stressed by a strongly 3D perturbation, then reconnection will occur quickly, releasing any stresses before they build up to large levels. This would be the situation in polar plumes. But if the system is stressed by a motion that keeps the system close to axisymmetric, then we expect that a large free energy will build up until the system spontaneously breaks the symmetry, most likely via an instability. In this case, we conjecture that a large fraction of the free energy will be released in a burst of reconnection. In order to test our conjectures we perform simulations, described below, in which we drive the field of Fig. 1 by an axisymmetric twist motion at the photospheric boundary. The simulations, however, are fully 3D so that even though the initial field and driving are axisymmetric analytically, the numerical system contains 3D perturbations and is free to adopt a 3D configuration if energetically favorable. As shown below, this system does produce the large burst of reconnection required to account for coronal jets.

3. The model

The numerical simulations reported in this paper were performed in a Cartesian domain, with x and y the horizontal axes and z the vertical axis, using the equations of ideal magnetohydrodynamics (MHD) with the magnetic forces expressed in the Lorentz rather

than the conservative form:

$$\frac{\partial \rho}{\partial t} + \nabla \cdot (\rho \mathbf{v}) = 0 \tag{1a}$$

$$\rho \frac{\partial \mathbf{v}}{\partial t} + \rho(\mathbf{v} \cdot \nabla)\mathbf{v} + \nabla P - \frac{(\nabla \times \mathbf{B}) \times \mathbf{B}}{\mu_0} = 0 \tag{1b}$$

$$\frac{\partial U}{\partial t} + \nabla \cdot (U\mathbf{v}) + P\nabla \cdot \mathbf{v} = 0 \tag{1c}$$

$$\frac{\partial \mathbf{B}}{\partial t} - \nabla \times (\mathbf{v} \times \mathbf{B}) = 0 \tag{1d}$$

where ρ is the plasma density, $\mathbf{B}$ and $\mathbf{v}$ the magnetic and velocity fields, P the plasma pressure, U the internal energy density, and $\mu_0 = 4\pi$ the magnetic permeability. The plasma is assumed to follow the ideal gas law, *i.e.*, $P = \rho RT$, with T the plasma temperature and R the gas constant. The internal energy density then obeys the relation $U = P/(\gamma - 1)$, where $\gamma = 5/3$ is the ratio of specific heats.

3.1. Initial Conditions

Our aim is to simulate the dynamics of the magnetic field in the highly conducting, low-pressure plasma of the inner corona. Consequently, we neglect gravity in the MHD equations, and assume initially uniform values for the coronal mass density ($\rho = 1$) and thermal pressure ($P = 10^{-2}$). The gas constant is $R = 10^{-2}$ and thus initially temperatures are uniformly $T = 1$ in the simulation domain. The homogeneity of the MHD equations allows us to scale our results for arbitrary mass, length, and time constants, each of which we choose to set to unity. The adiabatic sound speed then is $c_s = 0.13$. For the weak open background field, we assume a uniform vertical field $\mathbf{B}_v = -B_v \mathbf{e}_z$ with $B_v = 1$. Its associated Alfvén speed is $c_A = 0.28$, and the plasma beta (ratio of thermal to magnetic pressure) is $\beta = 0.25$. We add to this background the closed magnetic field of an embedded dipole of strength m_0 ($\mu_0 m_0/4\pi = 25$), that is oriented vertically and positioned below the bottom coronal boundary at $(0, 0, z_0 = -1.5)$. The resultant total vertical magnetic field is:

$$B_z(x, y, z) = \frac{\mu_0 m_0}{4\pi} \frac{2(z - z_0)^2 - (x^2 + y^2)}{(x^2 + y^2 + (z - z_0)^2)^{5/2}} - B_v. \tag{2}$$

This axisymmetric configuration at the bottom boundary ($z = 0$) consists of an intense positive magnetic polarity surrounded by weak negative fields as shown in Fig. 1. The total flux in this positive polarity is $\Phi = 30$, its maximum field strength is $|B|_{max} \approx 14$, its maximum Alfvén velocity is $c_A \approx 3.9$, and its minimum beta is $\beta \approx 1.3 \times 10^{-3}$. The polarity inversion line is located at radius $R_{pil} \approx 1.6$ from the center of the positive flux (located at the origin of our coordinate system).

The superposition of the uniform negative vertical magnetic field and the concentrated positive dipole field produce a magnetic null point ($\mathbf{B} = 0$) located on the symmetry axis $x = y = 0$ at height $z_n = (\mu_0 m_0/2\pi B_v)^{1/3} + z_0 \approx 2.2$. The field lines passing through the null form the well-known spine/fan topology of the magnetic field (Cowley 1974; Parnell et al. 1996; Longcope 2005), as shown in Fig. 1. In this axisymmetric geometry, the spine lines are vertical lines positioned along the symmetry axis, while the fan lines form a dome-shaped axisymmetric fan surface. For the simple fields assumed here, the fan surface is a section of a sphere satisfying

$$x_F^2 + y_F^2 + (z_F - z_0)^2 = (\mu_0 m_0/2\pi B_v)^{2/3} = 13.6 \tag{3}$$

for all points (x_F, y_F, z_F) on the fan. The intersection of the fan with the bottom boundary, the separatrix curve, is simply a circle of radius $r_F \sim 3.4$. As discussed above, the net magnetic flux within this circle vanishes exactly.

3.2. Boundary Conditions

We drive our initially axisymmetric configuration by imposing slow twisting motions at the bottom boundary of the domain, restricted to lie within the fan circle and also to follow the contours of B_z so as to leave its surface distribution unchanged in time. The imposed tangential velocity $\mathbf{v}_\perp(x, y, z = 0)$ is given by:

$$\mathbf{v}_\perp = v_0 f(t) \frac{B_r - B_l}{B_z} \tanh\left(k_B \frac{B_z - B_l}{B_r - B_l}\right) \mathbf{z} \times \boldsymbol{\nabla} B_z, \tag{4a}$$

$$\text{with} \quad f(t) = \frac{1}{2}\left[1 - \cos\left(2\pi \frac{t - t_l}{t_r - t_l}\right)\right], \tag{4b}$$

where the magnitude of the twisting motions, $v_0 = 3.7 \times 10^{-5}$ for $t \in [t_l, t_r]$ and $B_z \in [B_l, B_r]$. Note that v_0 vanishes at all other times and surface locations. We set $t_l = 100$ and $t_r = 1100$, to allow a brief period of relaxation of the initial state before switching on the motions. The cosine time profile allows a gradual acceleration from rest and deceleration to rest of the imposed flows. We also set $B_l = 0.1$ and $B_r = 13$, so that only the positive polarity flux is rotated. The resultant spatial profile has an approximately solid-body rotation of the positive flux near the axis, with a smooth but steep falloff to zero near the polarity inversion line, as shown in Fig. 2. Our objective is to accumulate slowly a large amount of free energy in the magnetic field, while delaying as long as possible the buildup of strong currents near the fan surface. The maximum velocity of the imposed twisting motions is about 1% of the local Alfvén speed.

We assume that the bottom boundary is closed by imposing a reflecting condition on the vertical velocity and zero gradient on all other quantities. The side boundaries are similarly closed and reflective, but free slip with regard to the tangential velocity. The top boundary is open with zero gradient conditions on all variables. We performed several tests to establish that the top and side boundaries are sufficiently far that they do not influence significantly the system evolution.

3.3. Numerics

We advance the MHD equations (1) in time using the *A*daptively *R*efined *M*agnetohydrodynamic *S*olver *(ARMS)*. *ARMS* is based on flux-corrected transport algorithms described in Devore (1991). The time-dependent equations are solved on a dynamically solution-adaptive grid administered by the adaptive mesh toolkit *PARAMESH* (MacNeice et al. 2000). *PARAMESH* divides the mesh into a hierarchy of sub-grids that cover the computational domain, allowing variation of the resolution within each sub-grid. It manages the relationships among the grids at different levels, particularly at refinement jumps occurring in the domain, imposes conservation constraints at such jumps, interpolates and projects the physical variables onto the various levels of grids, and balances the workload across the parallel compute processors assigned to the job.

We start with the nonuniform mesh as shown in Fig. 3. The total domain covers $[-12, +12] \times [-12, +12] \times [0, 24]$. The finest resolution is restricted to a central volume where the critical topological structures are found. This sub-volume, delimited by $[-7.5, +7.5] \times [-7.5, +7.5] \times [0, 13.5]$, is discretized by a $160 \times 160 \times 144$ uniform grid. The resolution there is equal to 0.09375. Outside this inner volume the resolution decreases by successive factors of two until the coarsest grid is reached at the top of the domain. The total number of grid blocks thus obtained is 7960, corresponding to about 4.1×10^6 grid cells. This is more than a factor of four smaller than the number required by a globally uniform mesh at the highest refinement level.

This initial grid refines and derefines adaptively during the simulation. For the simulations presented here, we set the adaptation criterion to be based on the ratio of the magnitude of electric current density relatively to the magnitude of the magnetic field. At sufficiently high values, the grid refines, while at sufficiently low values, the grid derefines, up or down to the prescribed limiting grid levels for the simulation. At each refinement (derefinement) of the mesh, the block and cell sizes are divided locally by 2 (0.5). At its peak, the number of grid blocks in the simulation below is approximately double the initial count, which is orders of magnitude less than the corresponding globally uniform mesh at

the highest refinement level.

The adaptive meshing adjusts the grid to resolve as finely as possible the thin current layers that drive and control the reconnection process. Although the resistive MHD terms are not included explicitly in the equations, numerical diffusion provides an effective resistivity in the model. The diffusion is particularly important where the gradients of the magnetic field are strong, i.e. at current sheets, and induces magnetic reconnection when the sheets reach the grid scale. This diffusion is minimized, and the onset of reconnection delayed, by maximizing the grid resolution in those regions. In the present simulation, we allowed a maximum refinement of three additional grid levels, or a factor of eight times the finest initial resolution. Thus, the smallest grid spacing reached in the current sheets is 1.2×10^{-2}.

4. Results

The primary result from our simulation is that the imposed slow boundary motions eventually lead to explosive dynamics and to a burst of energetic reconnection. Figure 4 shows the magnetic configuration (white and blue field lines) and the plasma density (yellow isosurface) at several times during the evolution. After some initial twisting of the closed field, the axisymmetry breaks down, leading to a large amount of reconnection between the closed and open fluxes. Note that the initially closed field lines, plotted in blue in Fig. 4, eventually become open, whereas some of the open field lines, plotted in white, become connected to the main positive polarity. This reconnection transfers energy and helicity from the closed to the open field and generates a jet. Plasma is accelerated upward and ejected through the top boundary and, hence, out of our simulation domain.

The time profile of the magnetic energy (see Fig. 5) shows three main phases to the evolution. **Energy build-up:** from $t = 0$ to $t \sim 920$ the magnetic energy increases smoothly as a result of the imposed boundary motions, but the system remains close to axisymmetric. **Energy release:** between $t \sim 920$ and $t \sim 1240$, the system undergoes a violent rearrangement in which a kink-like instability occurs that breaks the symmetry and allows copious reconnection to take place. The reconnection leads to the generation of a torsional Alfvén wave that drives upward plasma motions. **Energy relaxation:** after $t \sim 1240$ magnetic reconnection continues slowly, allowing the system to relax back down to a near-axisymmetric equilibrium that has much less twist than was injected by the boundary motions. This final state resembles the initial one, except that it does contain residual twist on low-lying field lines near the photospheric polarity inversion line. We discuss each of these evolutionary phases in more detail below.

4.1. Energy build-up

Since our system has low plasma beta throughout the evolution, the main contribution to the total energy is the magnetic energy. In order to minimize the effects of the boundaries, we selected the simulation box size to be substantially larger than the size of the enclosed bipole, consequently, the bulk of the total magnetic energy is due initially to the energy of the background field that occupies the bulk of the volume. This energy can be estimated as approximately equal to $VB_v^2/8\pi \simeq 548$, where V is the volume of the simulation box minus the volume enclosed by the fan. Since we measure the total initial magnetic energy to be 552, the contribution of the closed field is clearly small, but of course, most of the free energy is injected into this closed field.

During the first 100 time units no boundary driving motion is applied in order to allow the system to relax to a numerical equilibrium. Note that for the size scales and Alvén speeds given above, 100 time units corresponds to approximately one Alvén crossing time in the open-field region and 25 Alfvén times in the closed dipole region. Figure 5 shows that the kinetic energy stays vanishingly small, indicating that the system does achieve a robust numerical equilibrium.

Starting at $t = 100$, the photospheric twist is turned on, resulting in an almost linear increase of the magnetic energy (Fig. 5). The energy injection can be determined precisely by computing the Poynting flux $(\mathbf{B} \times \mathbf{v}_\perp) \times \mathbf{B}/\mu_0$ at the bottom boundary. It is evident from Fig. 6 that the Poynting flux profile follows the cosine shape of the time profile of the twisting motion. By integrating in time the Poynting flux, we find that 61 energy units have been injected in the numerical domain. The amount of free energy available (defined thereafter as the energy injected by the twisting motion) corresponds, therefore, to 11% of the total magnetic energy of the initial potential field.

In addition to energy, the twisting motions inject magnetic helicity into the system. The flux of helicity through the bottom boundary can be determined by computing the helicity density defined correctly in Pariat et al. (2005):

$$\frac{\mathrm{d}H}{\mathrm{d}t} = \frac{1}{2\pi} \int_{\mathcal{S}} \int_{\mathcal{S}'} \left(\frac{\mathbf{r}}{r^2} \times \frac{\mathrm{d}\mathbf{r}}{\mathrm{d}t} \right)_z B_z B'_z \, \mathrm{d}\mathcal{S} \, \mathrm{d}\mathcal{S}' \tag{5}$$

with $\mathbf{r} = \mathbf{x} - \mathbf{x}'$. Figure 6 shows that the total amount of helicity injected is about 1282. Given that the magnetic flux in the positive polarity spot is approximately equal to 30, and assuming a uniform twist for this flux, we derive that number of turns required to yield the injected helicity is equal to 1.4. This value agrees precisely with the the number of turn that we measure for the the twisted field lines at the time of the instability.

Although the boundary motions inject substantial energy and helicity to the system,

they impart negligible kinetic energy. As evident from Fig. 5, the kinetic energy shows no sign of increase throughout the energy build-up phase. On the other hand, the geometry of the system is clearly affected by the twist. Note that the initial potential field is purely 2D in that it has no azimuthal component. The effect of the twist is to generate azimuthal field and, thereby, increase the magnetic pressure inside the closed field region. This causes the closed field to expand outward in order to minimize its energy and to achieve a new force balance with the external field. Figure 7 shows the temporal variation of the height of the null point during this phase. We see that the height increases by a factor of almost 3. We also note that the expansion is primarily in the vertical direction. This is due to the vertical background field, which resists any horizontal deformation, but allows for free expansion in the vertical. As a result, the closed field region adopts an increasingly columnar geometry and begins to resemble a twisted flux tube. Of course the topology is not truly that of a twisted flux tube, because the structure has an end where it turns inside out, nevertheless, if the geometry becomes sufficiently extended, we expect that some of the physics of flux ropes will begin to apply.

Figure 7 also shows the evolution of the current density in the system. Since the plasma beta is small initially, and continues to decrease with increasing twist, the currents in the corona are almost completely field aligned, so that the field is force-free to a good approximation. Current flows up one leg of a field line and down the other so that there is no net current flowing in the corona. The currents close by flowing across the field on the bottom boundary, the photosphere. Note that there must be cross-field currents at the bottom boundary in order to maintain the magnetic stress there. This type of current structure is common to any low-beta system driven by footpoint motions (e.g. Antiochos & Devore 1999; MacNeice et al. 2004).

An important issue is the motion and deformation of the null point. Since the Lorentz force vanishes at the null, its position changes only as a result of velocities generated by gas pressure gradients or by viscous effects. Although we do not explicitly include viscosity in the simulation, some numerical viscosity must be present, but it stays small, because the null region is very well resolved during the initial evolution. Consequently, the null moves primarily as a result of gas pressure. Furthermore, the upward magnetic expansion deforms the null region into a disk-like shape. As can be seen in Fig. 7, a weak current sheet forms in this null-disk. This current is small compared to the large force-free currents due to the twist, nevertheless, it is significant and highly localized to the null disk. Note that since the plasma beta is large here, this current need not to be field-aligned and can close completely in the corona. The evolution of the null region in our simulation is the axisymmetric analogue to the classic translationally-symmetric current-sheet formation model described by Syrovatskii (1981).

The key difference between the axisymmetric and the translationally-symmetric systems is that we do not see any evidence for reconnection in the former, even for the large deformation evident in Fig. 7. The simulation confirms our arguments in Sect. 2 that reconnection cannot occur in an axisymmetric null-point system. It should be noted that this result holds even though our numerical system is not axisymmetric numerically. The symmetry is only in the analytic formulation of the initial field and drivers, we do not enforce it numerically. The axisymmetry is clearly broken by our simulation box with its square boundaries, and by the discretization on the Cartesian numerical grid. These departures from axisymmetry are small, because the boundaries are far and the system is well-resolved numerically, but they are definitely present. We conclude, therefore, that for twists below a certain limit, the system is stable to small, but finite 3D perturbations.

4.2. Energy Release

4.2.1. Initial Kink-Like Instability

As a result of the continued twisting and increasing vertical elongation of the dipolar field, the system eventually becomes unstable and collapses into a complex, highly 3D configuration. Once the system becomes 3D, it immediately undergoes violent reconnection with the external field, releasing a major fraction of its free energy and generating a large jet of plasma. We discuss the evolution in detail below.

It is evident from Fig. 4 that between $t = 920$ and $t = 940$ the axis of the magnetic structure starts to writhe. We believe that this instability is a form of the kink-mode. At the most basic level, the kink instability can be considered as simply the tendency of a flux tube to lower its energy by increasing its length. The total magnetic energy of a twisted flux tube can generally be broken up into the energy of the axial and the energy of the twist components. For fixed tube radius and fixed axial and twist (poloidal) flux, any stretching that increases the tube length will increase the energy in the axial field, but decrease the energy in the twist component. Therefore, the instability for kinking, or more generally, for axial stretching, becomes energetically favorable whenever the energy in the twist component begins to approach that in the axial.

In the particular simulation presented in this paper, the instability occurs when the number of turns within the magnetic structures reaches approximately 1.4 turns (Note the number of turns of the green field line around the inner spine in Fig. 7; bottom left panel). By this time ($t = 920$), 1230 helicity units have been injected into the corona and the total magnetic energy is equal to 610, which implies a free magnetic energy $\sim 10\%$ of the initial

magnetic energy. This is significantly larger than the energy of the initial closed field as estimated above. In order to determine the sensitivity of the instability to these values, we performed several simulations using different sets of parameters that affect the amount of injected twist. We changed independently the intensity of the twisting motion v_0 (see Eq. 4a), the duration of the twisting motion t_r, the intensity of the inner dipole m_0 and also the radial profile of the twisting motion (we used a sinusoidal profile). The results of these different simulations are displayed in Fig. 8.

Note that no instability occurs if the injected free energy is below 51 units, the twisting angle under 2.6π (the field lines have 1.3 turns around the inner spine), and the helicity lower than 1080. It is not possible from this coarse parameter study to determine an exact instability threshold for our physical system, but it is clear that a threshold does exists above which the magnetic configuration becomes unstable. Below this threshold our simulation appears to maintain a stable equilibrium for many Alfvén crossing times, even though the numerics do introduce 3D noise to the system. The existence of such a threshold is the most compelling evidence that an ideal kink-like instability is the physical mechanism for the observed writhing. Note, however, that this ideal instability does not directly drive the jet; nor is it likely to release much energy, although this claim needs to be tested with a truly non-resistive code. It is primarily the reconnection allowed by the breaking of the axisymmetry, that is responsible for the strong dynamics in our model.

4.2.2. Reconnection Driven Dynamics

Once the axisymmetry is broken, reconnection dominates all subsequent evolution. The system's behavior is physically similar to that of a resistive kink, as in the classic Kadomtsev (1975) theory for tokamak disruptions, in that the feedback between an ideal and a resistive mode produces an explosive burst of energy release. In our case, the bulk of the energy release is due to the propagation of a nonlinear torsional Alfvén waves out the top of the simulation box. These waves are produced by the interchange reconnection of a highly twisted closed field line with an untwisted open field line. Since the initial twisted field line is force-free, the twist is distributed uniformly along that field line. As a result of reconnection the open and closed lines exchange sections, resulting in a new pair of open and closed field lines. Each of these post-reconnection lines consists of a twisted and untwisted section and, hence, is far from force balance. Note that since twist is a measure of helicity, it must be conserved under reconnection. In order to re-establish force balance the twist propagates from the twisted to the untwisted section in both reconnected field lines. In the new closed field line this results in a nonlinear Alfvén wave that bounces back and forth between the two

photospheric footpoints, but in the new open field line the wave simply propagates out the top of the box and is lost to the system. We saw this type of evolution in our previous translationally-symmetric calculations (e.g. Karpen et al. 1996, 1998). The only difference in this case is that one of the flux systems is open, allowing a large fraction of the helicity to escape the simulation volume. The outwardly propagating nonlinear Alfvén waves can be seen in Fig. 4. They appear as kinks in the blue field lines that used to be closed, but are opened by reconnection.

As the waves propagate out their pressure gradients push the plasma, resulting in the extended jet of upward moving material evident in Fig. 4. A vertical cut through this jet, Fig. 9, indicates that the jet extends to the top of the simulation box. The right panels in Fig. 9 show the vertical velocity distribution at several times in the simulation. The collimated column of mostly-vertical high velocities tends to be co-spatial with the location of higher plasma density. Although the initial plasma acceleration is due to the slingshot effect in the reconnection region, itself, this process is not the main driver of our extended jet. The well-known "jets" associated with reconnection regions can be seen during the initial stage of the energy release (at $t = 980$ and $t = 1040$) as diverging flows from the reconnection point in Fig. 9). Note that these reconnection-region jets are directed both upward and downward, whereas our extended, coronal-hole jet is directed only upward. As discussed above, the extended jet is driven primarily by the release of the closed-field twist onto open field lines, resulting in continuous upward momentum deposition by nonlinear MHD waves.

The maximum plasma velocities in the simulation reach 0.28, roughly the Alfvén velocity c_A in the open field, and occur in the reconnection-region jets. Such velocities are predicted by almost all models of reconnection. The velocities of our extended polar jet range between 0.18-0.27 (0.65-0.9c_A), which are clearly supersonic. The jet propagates near the speed of the torsional Alfvén wave, approximately the local Alfvén velocity. We should note, however, that since gravity is not included in this simulation, the upward velocities are somewhat overestimated in the model. On the other hand, the gas pressure difference between closed field and open-field plasma is also not included, and this would have the effect of enhancing the upward velocities.

A key feature of our model jet is that it has an enhanced density compared to the surrounding plasma. This results is evident in Fig. 4, which plots the plasma density isocontour $\rho = 1.25$, i.e., a density higher by 25% than the initial uniform density. The jet is clearly evident as a region of increased density. The plasma density in the jet reaches nearly twice the initial density, while the temperatures are enhanced by a factor of approximately 1.4. Polar jets on the Sun exhibit much higher densities than surrounding open-field material,

because they involve the release of high-density closed-field plasma onto open field lines. In our simulation the initial density and temperature are uniform throughout, and since the closed field region expands substantially, the density and temperature of the closed-field region actually drops below the surrounding open-field plasma. This verifies that the driver of the jet in our simulation cannot be gas pressure. The density enhancements in our jet are due to the compression of open-field plasma by the sideways expansion of newly reconnected open field. The compression of the plasma follows the magnetic field oscillations and, hence, the jet adopts the helical shape of the Alfvén wave (see Fig. 4). This helical structure for the jet is an important prediction of our model and should be evident in multi-viewpoint observations (Patsourakos et al. submitted)

Another important property of the jet is that it has a great deal of fine-scale internal structure. This can be seen in Fig. 9 which shows a 2D cut (the $x = 0$ plane) of the electric currents and vertical velocities in the simulation box. Note that at any instant the high-current regions take on an "Eiffel tower" or "inverse Y" shape. For the grids used in this simulation we find that the width of the jet structure is approximately 20% of the size of the closed field region, but structures clearly develops down to the scale of the grid.

As the reconnection progresses, the outer spine flux migrates with the continued writhing of the closed field. Observed from the side, therefore, the jet appears to show a drift. The jet moves a length scale of order the closed magnetic field in a time scale of 100 time units. The velocity of this drift is approximately $5 \times 10^{-2} \sim 0.2c_A$, about one fifth to one tenth of the upward velocities found in the jet itself. We emphasize that this drift is not a real material motion. It is only a phase velocity due to the migration of the reconnection region to different flux surfaces. Again the situation is similar to the translationally symmetric case where we saw that reconnection led to the formation of a large loop-like volume of filled with thin current sheets down to the grid scale (Karpen et al. 1996). Reconnection in this open field case leads to the formation of a large volume filled with fine-scale currents and upflows. This small-scale structure for the jet is another prediction of our model.

4.3. Energy and helicity budgets

The previous section focused on the detailed dynamics during the energy release phase of the simulation, because the dynamics are critical for comparing the model with jet observations. In this section we consider the evolution of global quantities such as energy and helicity, which are critical for understanding the general properties of the model and for determining its implications for the solar wind.

4.3.1. Energy Evolution

We note from Fig. 5 that the photospheric motions inject approximately 60 units of free magnetic energy into the corona (see Sect.4.1). During the release phase, a total of 55 energy units are lost in less than 200 time units (from ~ 820 at $t = 1000$ to ~ 765 at $t = 1200$), so that only 5 units of the free energy (less than 10%) remain in the system. Most of the energy losses are due to the magnetic energy, which decreases by 51 units, see Fig. 5). The internal energy decreases by 5 units, while the kinetic energy experiences a net gain of only 1 unit between $t = 1000$ and $t = 1200$, but undergoes large variations (of order 5 energy units) during this evolutionary phase.

Note that although the decrease in total magnetic energy is only 8.2% of the maximum magnetic energy, it corresponds to more than 83% of the stored free energy! We conclude, therefore, that the kink-like instability and series of reconnections that take place during the dynamic phase are extremely efficient at releasing the injected free magnetic energy and converting it to other forms. Since our simulation neglects gravity and solves the ideal MHD equations, there are only three modes of conversion for the magnetic free energy: Alfvén waves that escape out the top, plasma kinetic energy, and numerical dissipation. It should be noted that the energy that is dissipated by the numerical diffusion, whether magnetic or kinetic, is lost to the system and does not appear as heat (internal energy). Consequently, our simulation tends to underestimate the plasma temperature, but since the system is low beta, we do not expect this to have a significant effect on the evolution. Furthermore, a proper treatment of the temperature would require accurate calculation of radiative losses and field-aligned thermal conduction, which is beyond the scope of this paper.

It is evident from Fig. 5 that the kinetic energy undergoes a sharp increase just after the start of the instability. This increase of 5 energy units is due to the acceleration of plasma during the kink-like instability, the reconnection, and the nonlinear Alfvén wave driving of the jet. The kinetic energy then decreases either by plasma transport through the top boundary or by numerical dissipation.

In order to track the amount of energy transported away, we computed the energy flux through horizontal planes ($z = const.$) in the simulation box by integrating the kinetic flux density $1/2 v_z \rho v^2$ and the Poynting flux density $-((\mathbf{v} \times \mathbf{B}) \times \mathbf{B}) \cdot \mathbf{e}_z / \mu_0$, over these horizontal planes. The fluxes along with their time integral are shown in Fig. 10. We see from this figure that, as expected, the magnetic flux through the bottom boundary decreases smoothly to zero by the end of the driving ($t = 1000$), but that large impulses of magnetic and kinetic energy flux occur high in the simulation domain during the energy release phase.

A substantial fraction of the free magnetic energy is used to generate the torsional waves

and is transported away by the waves. In Fig. 10 (top row), we note that 14 energy units are ejected in the form of Poynting flux. This is the magnetic energy transported within the jet. In our simulation this energy is simply lost to the system, but on the Sun, available to drive the solar wind. The nonlinear wave can transport the energy in the upper corona and, when dissipated, can accelerate the solar wind (Cranmer & van Ballegooijen 2005). Our results, therefore, support the models which argue that reconnection between small bipoles and open field is responsible for heating and accelerating the wind (e.g. Axford & McKenzie 1992; Fisk et al. 1999)

The jet also expels 2.5 energy units in the form of kinetic energy (see Fig. 10, bottom row), some of which originated in the reconnection sites and some driven by the waves. In total, the jet expels approximately 20 energy units, which represent 1/3 of the injected free energy. The amount of kinetic energy dissipated within the numerical domain is approximately 2.5. We find, therefore, that about half the free magnetic energy is lost through numerical dissipation. In principle, this energy would be available for plasma heating, but as emphasized above, an accurate treatment of the plasma energetics would require full inclusion of additional energy loss mechanisms.

4.3.2. Helicity Evolution

In addition to energy, a key global quantity is magnetic helicity, because this is expected to be conserved during reconnection (Woltjer 1958). In his seminal paper, Taylor (1974) argued that "unrestricted" reconnection would result in the final equilibrium state being that of a linear force-free field. Our system, however, does not undergo unrestricted reconnection, because the reconnection is confined to the separatrix boundary between the open and closed flux systems (e.g. Antiochos et al. 2002). For this open system in which helicity can escape, the Taylor state corresponds to the initial potential field, so this theory is not expected to apply directly.

Nevertheless, it is interesting to note from Fig. 4 that the closed field flux does experience, at least, two reconnections. The first and last panels of the figure show that almost all the closed flux returns to its initial closed state and the open back to open. This requires that all the flux undergo an even number of interchange reconnections during the evolution. The only significant difference between the initial and final states is that the amount of helicity/twist contained in the closed-flux domain is much lower than the amount injected. Field lines are far less twisted in the final panels of Fig. 4 than just before the trigger of the instability.

In order to quantify the helicity loss we plot, as above, the helicity flux at several heights in the simulation box (see Fig. 11). All the helicity is injected into the closed field region only, but we find that due to interchange reconnection most of this helicity is transferred from the closed to the open and, thereby, ejected. Figure 11 shows that approximately 1150 units of helicity exit the top open boundary, which is about 90% of the helicity injected through the bottom boundary. The bulk of the remaining helicity stays in the system in the form of the weakly twisted closed-field lines deep within the embedded dipole. It seems unlikely that the low-lying closed flux near the polarity inversion line can come into contact with open flux and release its helicity. In fact, it is surprising how much of the helicity does escape. Releasing 90% of the helicity requires extreme distortions of the topology so that flux from well inside the initially closed region comes into contact with open field and reconnects.

It is also interesting to note that in spite of the copious reconnection in the system, and the substantial numerical diffusion, the simulation conserves helicity to a high accuracy. In previous 2.5D simulations with fixed numerical grids (MacNeice et al. 2004), we found that helicity is conserved only if the number of grid points were sufficiently large. It is not possible to have equivalently dense grids in this fully 3D simulation; therefore, our results show the importance of using an adaptive mesh, as in our simulation here, for the proper treatment of 3D reconnection.

4.4. Relaxation

The relaxation phase of the evolution $t \sim 1180$ to ~ 1500 is characterized by a slow reconnection that attempts to return the fan and spines to their current-free state in Fig. 1. However, the system cannot return to a true potential field, because there is still some residual twist on low-lying field lines near the PIL. This twist is on flux far from the open field region; consequently, it cannot be released via reconnection and propagation out the top. The low-lying non-potential flux quickly achieves a near force-free equilibrium after the impulsive release phase, and shows minimal evolution thereafter, except for a very slow dissipation of the currents due to the numerical resistivity. Since we resolve the structures very well numerically, the effective Reynolds number is large (over 10^4), so the amount of dissipation of these volumetric currents during the relaxation phase is negligible.

The effect of the long-lived volumetric currents is to force the existence of a current sheet at the separatrix. It is evident from Fig. 4 that by the end of the simulation the system is not in an axisymmetric state. In fact, once the symmetry is broken in our simulation, it is effectively impossible for the system to return to an axisymmetric state. But for the flux

distribution on the photosphere, the axisymmetric state is the only one that has no stress at the separatrix. We conclude, therefore, that current sheets at the separatrix are essentially an inevitable consequence of the embedded bipole topology of Fig. 1. Note that this conclusion must hold for the Sun, as well. Every embedded bipolar region in a coronal hole (or elsewhere) will have a current sheet at its separatrix, which has important implications for plasma heating and energization.

Figure 12 shows the current and velocity structure at the separatrix late in the relaxation phase of the simulation $t = 1360$. We note that a current sheet is clearly evident on the fan surface and that strong current lines are present along the spines. The topology closely resembles the model presented in Antiochos (1996) for a stressed 3D null point. As a result of the stress, the inner (blue field-line bundle in the figure) and outer (white) spine lines are displaced from each other and the fan breaks up into an inner (blue field lines) and an outer (white field lines) surfaces that no longer line up, as in the initial potential state. This mismatch of the fans implies that a current sheet is present, which is strongest along a line (a finite-length null line) joining the two spines (see Antiochos 1996, for details). An isosurface of very low field strength is plotted in Figure 12, clearly showing that the null point has deformed to an extended linear structure lying between the two spines.

Figure 12 also shows that magnetic reconnection is occurring at this "null-line" current sheet. We note the classic stagnation point flows with outflowing velocities of order the Alfvén speed, that are associated with all reconnection models (e.g. Sweet 1958; Parker 1957; Petschek 1964). Note also, the importance of having an adaptive grid in order to resolve the reconnection region. We find that the reconnection resembles the Sweet-Parker configuration, which has an extended current sheet. The effect of the reconnection is to attempt to bring the two spines back into alignment (Antiochos et al. 2002), but as stated above, this is not possible due to the stress remaining in the system. We expect, therefore, that the system will eventually settle into a quasi-static equilibrium similar to that of Figure 12, but with a smaller current sheet that is supported by gas pressure. Of course, any motion at the photosphere will result in further reconnection at this current sheet and continued heating of the plasma near the fan and spines, which may play an important role in heating the solar wind and in the formation of plumes (e.g. Wang 1998). We conclude, therefore, that our model may be important for understanding not only jets, but much of the activity observed in coronal holes.

5. Discussion

5.1. Conclusions

We performed a 3D Cartesian MHD numerical simulation of the interchange reconnection between closed and an open fields using the *A*daptively *R*efined *M*agnetohydrodynamic *S*olver *(ARMS)*. We assumed the simplest possible multipolar topology of an axisymmetric bipole in a uniform background open field, and drove the system with a slow axisymmetric rotation at the photosphere. The main results and implications of our simulation are the following:

1. **Reconnection cannot occur in an axisymmetric null-point topology**. As long as the system stayed close to axisymmetry, the photospheric motions drove a slow build-up of free energy in the corona with no evidence for any energy loss, even though current sheets appeared at the separatrix surface.

2. **A kink-like instability can trigger fast energy release in an embedded bipole topology.** Beyond a certain critical twist/helicity, the approximately axisymmetric system became unstable to a 3D kink-like mode that broke the symmetry and immediately induced reconnection. The system, therefore, exhibits the "switch-on" characteristic required for explosive energy release in the corona.

3. **3D reconnection is extremely efficient at releasing the free energy stored in an embedded bipole topology.** Approximately 83% of the free energy was liberated by reconnection, with roughly one third converted to nonlinear Alfvén waves that propagated out the top of the simulation domain and the rest dissipated in fine-scale currents sheets that formed throughout the volume. Almost all the helicity, $\sim 90\%$ was ejected.

4. **A high-speed (Alfvénic), massive jet is generated by impulsive reconnection.** Interchange reconnection transferred the twist from closed to open field lines, thereby producing a large flux of nonlinear torsional Alfvén wave that compressed, heated, and accelerated plasma upward. This jet mechanism has been previously called *magnetic twist jet* (Shibata et al. 1997). Reconnection is the key mechanism that generates the jet in our model.

5. **Current sheets persist at the open-closed field interface long after the impulsive energy release.** The presence of long-lived residual twist deep in the closed field region implies that current sheets and the accompanying reconnection must persist at the separatrices in the system, the fan and spines. The topology of these current

sheets resembles that proposed in Antiochos (1996) and the reconnection is strikingly similar to the classic Sweet-Parker model. These long-lived current sheets may play an important role in heating and accelerating the wind.

5.2. Application to polar jets

X-ray jets, defined as transitory X-ray brightenings in the corona with apparently collimated motions, were discovered by the Soft X-ray Telescope on *Yohkoh* (Tsuneta et al. 1991; Shibata et al. 1992; Shibata & Murdin 2000). Recently X-ray jets have received increased attention, because the X-ray telescope on *Hinode* has found that the jets are an order of magnitude more frequent than previously believed (Cirtain et al. 2007). They are especially common in corona holes, where they are believed to be due to the interaction between open and closed field (e.g. Shibata et al. 1992). Previous simulations (Yokoyama & Shibata 1995, 1996; Miyagoshi & Yokoyama 2004; Archontis et al. 2005, 2006; Isobe et al. 2006, 2007; Moreno-Insertis et al. 2008) have demonstrated that evaporation flows can explain many of the properties of X-ray jets, but this mechanism cannot account for the helical structure and Alfvénic velocities observed in some polar hole jets (Patsourakos et al. submitted). The 3D MHD simulation presented in this paper is the first to demonstrate clearly that the release of magnetic twist onto open field lines by magnetic reconnection leads to the generation of a high velocity jet. Unlike earlier 2D simulations Shibata & Uchida (1985, 1986), reconnection plays the central role in the generation of the jet in our model.

Although the purpose of this paper was to demonstrate the basic mechanism and not to compare the simulation directly with observations, it should be noted that the parameters for the simulation are compatible with typical solar values. Assuming a coronal density of 10^{-13} kg m^{-3} and a pressure of 10^{-3} Pa implies a temperature of 1.2×10^6 K. Taking the uniform field in the coronal hole to be 5 G and assuming a unit length of 10 Mm, implies that the embedded polarity region has a diameter of 33 Mm, a maximum field intensity $|\mathbf{B}|$ of 69 G and a flux of 1.5×10^{20} Mx. For these parameters the Alfvén speed in the corona is equal to 1.4×10^3 km s^{-1}, the time unit is equal to 2 s, and the energy unit equals 2.5×10^{21} J. The total amount of free energy injected is thus of 1.5×10^{23} J. Therefore, our *magnetic twist jet* has a velocity up to 1200 km s^{-1}. A total energy of order of 5×10^{22} J is ejected through the top boundary, $\sim 3/4$ of it being transported away by the nonlinear Alfvén wave. The temperature within the jet is approximately 1.7×10^6 K and the density approximately 2×10^{-13} kg m^{-3}. These values lie within the range of observed properties of jet, except that our jet tends to be under-dense and somewhat cool, primarily because of the neglect of joule heating in the simulation. We expect that if the large amount of energy lost

by dissipation had been included as a heating term in the model, the temperatures would have reached observed values. Furthermore, our model reproduces several classic geometrical features observed in jets, including the "inverse-Y/Eiffel tower" shape, the drift of the jet axis, the 3D helical structures (Patsourakos et al. submitted), and the recent observation of Alfvén wave within polar hole jets (Cirtain et al. 2007; Savcheva et al. 2007).

A critical issue for the model is obviously the assumption of axisymmetry. Of course, magnetic structures on the Sun are always fully 3D. The key role of the axisymmetry in our model is to suppress the reconnection until a large amount of free energy has built up, and then to release it explosively via a quasi-ideal instability that induces reconnection. We claim that even for a fully 3D system, as long as the magnetic configuration is not too distorted from that of Fig. 1, this basic physical process will still occur. This conjecture will be explored in future work.

E.P. wish to thank Mark Linton, Igniacio Ugarte-Urra and Fernando Moreno-Insertis for useful discussions. This work was supported, in part, by the NASA HTP, TR&T, and SR&T programs.

REFERENCES

Antiochos, S. K. 1987, ApJ, 312, 886

Antiochos, S. K. 1996, in Astronomical Society of the Pacific Conference Series, Vol. 95, Solar Drivers of the Interplanetary and Terrestrial Disturbances, ed. K. S. Balasubramaniam, S. L. Keil, & R. N. Smartt, 1

—. 1998, ApJ, 502, L181

Antiochos, S. K., & Devore, C. R. 1999, in Measurement Techniques in Space Plasmas Fields, ed. M. R. Brown, R. C. Canfield, & A. A. Pevtsov, 187

Antiochos, S. K., Karpen, J. T., & DeVore, C. R. 2002, ApJ, 575, 578

Archontis, V., Galsgaard, K., Moreno-Insertis, F., & Hood, A. W. 2006, ApJ, 645, L161

Archontis, V., Hood, A. W., & Brady, C. 2007, A&A, 466, 367

Archontis, V., Moreno-Insertis, F., Galsgaard, K., & Hood, A. W. 2005, ApJ, 635, 1299

Axford, W. I., & McKenzie, J. F. 1992, in Solar Wind Seven Colloquium, ed. E. Marsch & R. Schwenn, 1–5

Brueckner, G. E., & Bartoe, J.-D. F. 1983, ApJ, 272, 329

Canfield, R. C., Reardon, K. P., Leka, K. D., Shibata, K., Yokoyama, T., & Shimojo, M. 1996, ApJ, 464, 1016

Cirtain, J. W., Lundquist, L. L., DeLuca, E. E., Savcheva, A., Shimojo, M., & Tsuneta, S. 2007, in American Astronomical Society Meeting Abstracts, Vol. 210, American Astronomical Society Meeting Abstracts

Cowley, S. W. H. 1974, Journal of Plasma Physics, 12, 319

Cranmer, S. R., & van Ballegooijen, A. A. 2005, ApJS, 156, 265

de Pontieu, B., Berger, T. E., Schrijver, C. J., & Title, A. M. 1999, Sol. Phys., 190, 419

Devore, C. R. 1991, Journal of Computational Physics, 92, 142

Fisk, L. A., Zurbuchen, T. H., & Schwadron, N. A. 1999, ApJ, 521, 868

Golub, L., Deluca, E., Austin, G., Bookbinder, J., Caldwell, D., Cheimets, P., Cirtain, J., Cosmo, M., Reid, P., Sette, A., Weber, M., Sakao, T., Kano, R., Shibasaki, K., Hara, H., Tsuneta, S., Kumagai, K., Tamura, T., Shimojo, M., McCracken, J., Carpenter, J., Haight, H., Siler, R., Wright, E., Tucker, J., Rutledge, H., Barbera, M., Peres, G., & Varisco, S. 2007, Sol. Phys., 243, 63

Golub, L., Krieger, A. S., Silk, J. K., Timothy, A. F., & Vaiana, G. S. 1974, ApJ, 189, L93

Gurman, J. B., Thompson, B. J., Newmark, J. A., & Deforest, C. E. 1998, in Astronomical Society of the Pacific Conference Series, Vol. 154, Cool Stars, Stellar Systems, and the Sun, ed. R. A. Donahue & J. A. Bookbinder, 329

Harrison, R. A., Harra, L. K., Brković, A., & Parnell, C. E. 2003, A&A, 409, 755

Harvey, K. L. 1993, PhD thesis, , Univ. Utrecht, (1993)

Innes, D. E., Inhester, B., Axford, W. I., & Willhelm, K. 1997, Nature, 386, 811

Isobe, H., Miyagoshi, T., Shibata, K., & Yokoyama, T. 2006, PASJ, 58, 423

Isobe, H., Tripathi, D., & Archontis, V. 2007, ApJ, 657, L53

Jiang, Y. C., Chen, H. D., Li, K. J., Shen, Y. D., & Yang, L. H. 2007, A&A, 469, 331

Kadomtsev, B. B. 1975, Soviet Journal of Plasma Physics, 1, 710

Karpen, J. T., Antiochos, S. K., & Devore, C. R. 1996, ApJ, 460, L73

Karpen, J. T., Antiochos, S. K., Devore, C. R., & Golub, L. 1998, ApJ, 495, 491

Lau, Y.-T., & Finn, J. M. 1990, ApJ, 350, 672

Longcope, D. W. 2005, Living Reviews in Solar Physics, 2, 7

MacNeice, P., Antiochos, S. K., Phillips, A., Spicer, D. S., DeVore, C. R., & Olson, K. 2004, ApJ, 614, 1028

MacNeice, P., Olson, K. M., Mobarry, C., de Fainchtein, R., & Packer, C. 2000, Computer Physics Communications, 126, 330

McKenzie, J. F., Banaszkiewicz, M., & Axford, W. I. 1995, A&A, 303, L45

Miyagoshi, T., & Yokoyama, T. 2004, ApJ, 614, 1042

Moreno-Insertis, F., Galsgaard, K., & Ugarte-Urra, I. 2008, ApJ, 673, L211

Pariat, E., Démoulin, P., & Berger, M. A. 2005, A&A, 439, 1191

Parker, E. N. 1957, J. Geophys. Res., 62, 509

——. 1958, ApJ, 128, 664

——. 1983, ApJ, 264, 642

Parnell, C. E., Smith, J. M., Neukirch, T., & Priest, E. R. 1996, Physics of Plasmas, 3, 759

Patsourakos, S., Pariat, E., Vourlidas, A., Antiochos, S. K., Howard, R., Moss, D., & Wuelser, J. P. submitted, ApJ

Pérez, M. E., & Doyle, J. G. 2000, A&A, 360, 331

Petschek, H. E. 1964, in The Physics of Solar Flares, ed. W. N. Hess, 425

Priest, E. R., Titov, V. S., Vekestein, G. E., & Rikard, G. J. 1994, J. Geophys. Res., 99, 21467

Savcheva, A., Cirtain, J., Deluca, E. E., Lundquist, L. L., Golub, L., Weber, M., Shimojo, M., Shibasaki, K., Sakao, T., Narukage, N., Tsuneta, S., & Kano, R. 2007, PASJ, 59, 771

Schrijver, C. J., & Title, A. M. 2002, Sol. Phys., 207, 223

Schrijver, C. J., Title, A. M., van Ballegooijen, A. A., Hagenaar, H. J., & Shine, R. A. 1997, ApJ, 487, 424

Shibata, K., Ishido, Y., Acton, L. W., Strong, K. T., Hirayama, T., Uchida, Y., McAllister, A. H., Matsumoto, R., Tsuneta, S., Shimizu, T., Hara, H., Sakurai, T., Ichimoto, K., Nishino, Y., & Ogawara, Y. 1992, PASJ, 44, L173

Shibata, K., & Murdin, P. 2000, Encyclopedia of Astronomy and Astrophysics

Shibata, K., Nitta, N., Strong, K. T., Matsumoto, R., Yokoyama, T., Hirayama, T., Hudson, H., & Ogawara, Y. 1994, ApJ, 431, L51

Shibata, K., Shimojo, M., Yokoyama, T., & Ohyama, M. 1997, in Astronomical Society of the Pacific Conference Series, Vol. 111, Magnetic Reconnection in the Solar Atmosphere, ed. R. D. Bentley & J. T. Mariska, 29

Shibata, K., & Uchida, Y. 1985, PASJ, 37, 31

—. 1986, Sol. Phys., 103, 299

Shimojo, M., Hashimoto, S., Shibata, K., Hirayama, T., Hudson, H. S., & Acton, L. W. 1996, PASJ, 48, 123

Shimojo, M., Narukage, N., Kano, R., Sakao, T., Tsuneta, S., Shibasaki, K., Cirtain, J. W., Lundquist, L. L., Reeves, K., & Savcheva, A. 2007, PASJ, 59, 745

Shimojo, M., & Shibata, K. 2000a, Advances in Space Research, 26, 449

—. 2000b, ApJ, 542, 1100

Shimojo, M., Shibata, K., & Harvey, K. L. 1998, Sol. Phys., 178, 379

Sweet, P. A. 1958, in IAU Symposium, Vol. 6, Electromagnetic Phenomena in Cosmical Physics, ed. B. Lehnert, 123

Syrovatskii, S. I. 1981, ARA&A, 19, 163

Taylor, J. B. 1974, Physical Review Letters, 33, 1139

Tsuneta, S., Acton, L., Bruner, M., Lemen, J., Brown, W., Caravalho, R., Catura, R., Freeland, S., Jurcevich, B., & Owens, J. 1991, Sol. Phys., 136, 37

Wang, Y. M. 1998, ApJ, 501, L145

Wang, Y.-M., & Muglach, K. submitted, ApJ

Wang, Y.-M., & Sheeley, Jr., N. R. 2002, ApJ, 575, 542

Wang, Y.-M., Sheeley, Jr., N. R., Socker, D. G., Howard, R. A., Brueckner, G. E., Michels, D. J., Moses, D., St. Cyr, O. C., Llebaria, A., & Delaboudinière, J.-P. 1998, ApJ, 508, 899

Woltjer, L. 1958, Proceedings of the National Academy of Science, 44, 489

Yamauchi, Y., Moore, R. L., Suess, S. T., Wang, H., & Sakurai, T. 2004, ApJ, 605, 511

Yokoyama, T., & Shibata, K. 1995, Nature, 375, 42

——. 1996, PASJ, 48, 353

This preprint was prepared with the AAS LaTeX macros v5.2.

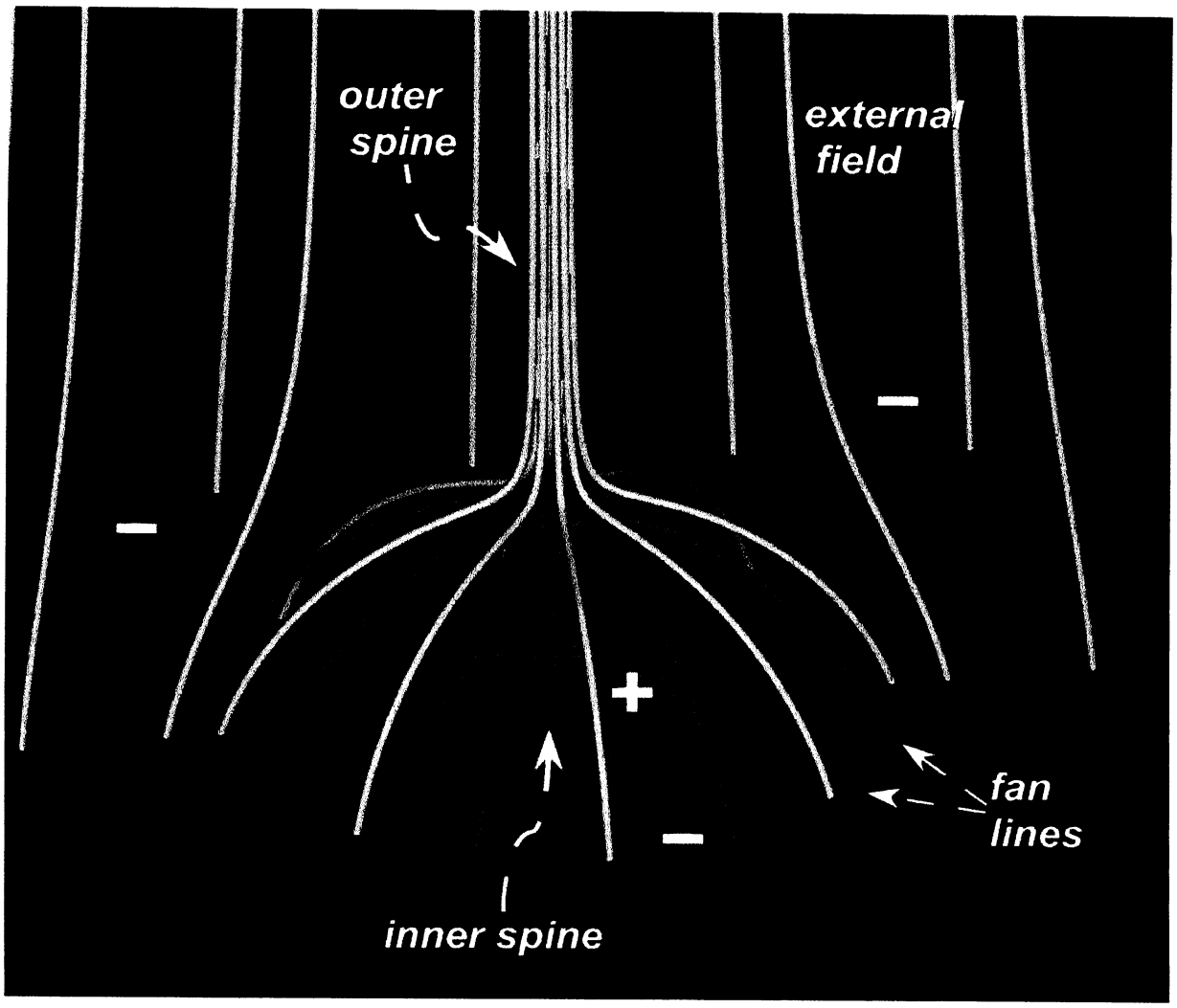

Fig. 1. 3D view of the initial magnetic configuration. The distribution of the magnetic field intensity $|\mathbf{B}|$ at the $z = 0$ bottom (photospheric) plane is color-shaded; [purple; blue; cyan; green; yellow; red] correspond to field intensity equal to [12.5;10;7.5;5;2.5;0] respectively. The black dashed circle on this plane corresponds to the polarity inversion line (PIL). Field lines belonging to the inner connectivity (closed) domain are plotted in cyan, while those belonging to the outer connectivity (open) domain are displayed in white.

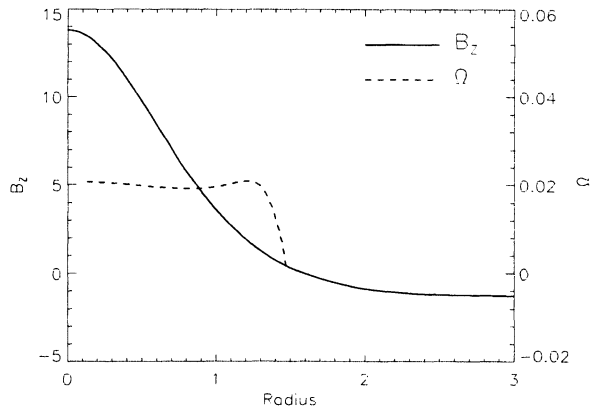

Fig. 2. Radial profiles of the vertical magnetic field B_z and the angular velocity Ω at the bottom boundary (photospheric) plane.

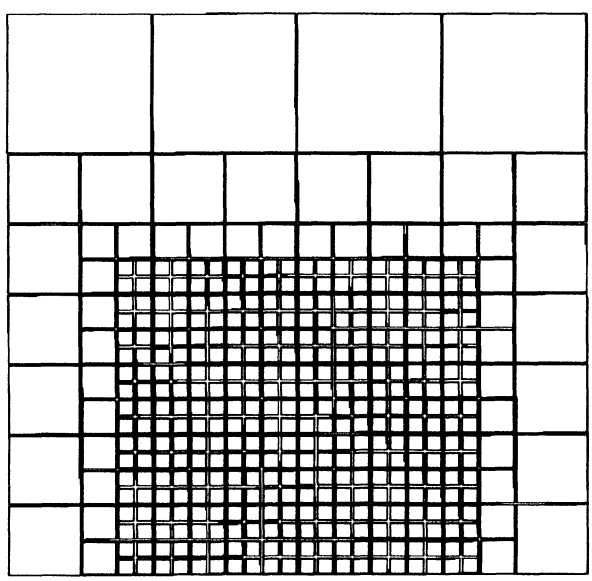

Fig. 3. 2D vertical slice of the initial mesh in the (xz) plane, with $x \in [-12 : +12]$ and $z \in [0 : 24]$. The mesh in y is identical to that in x. Each block consists of 8^3 grid cells.

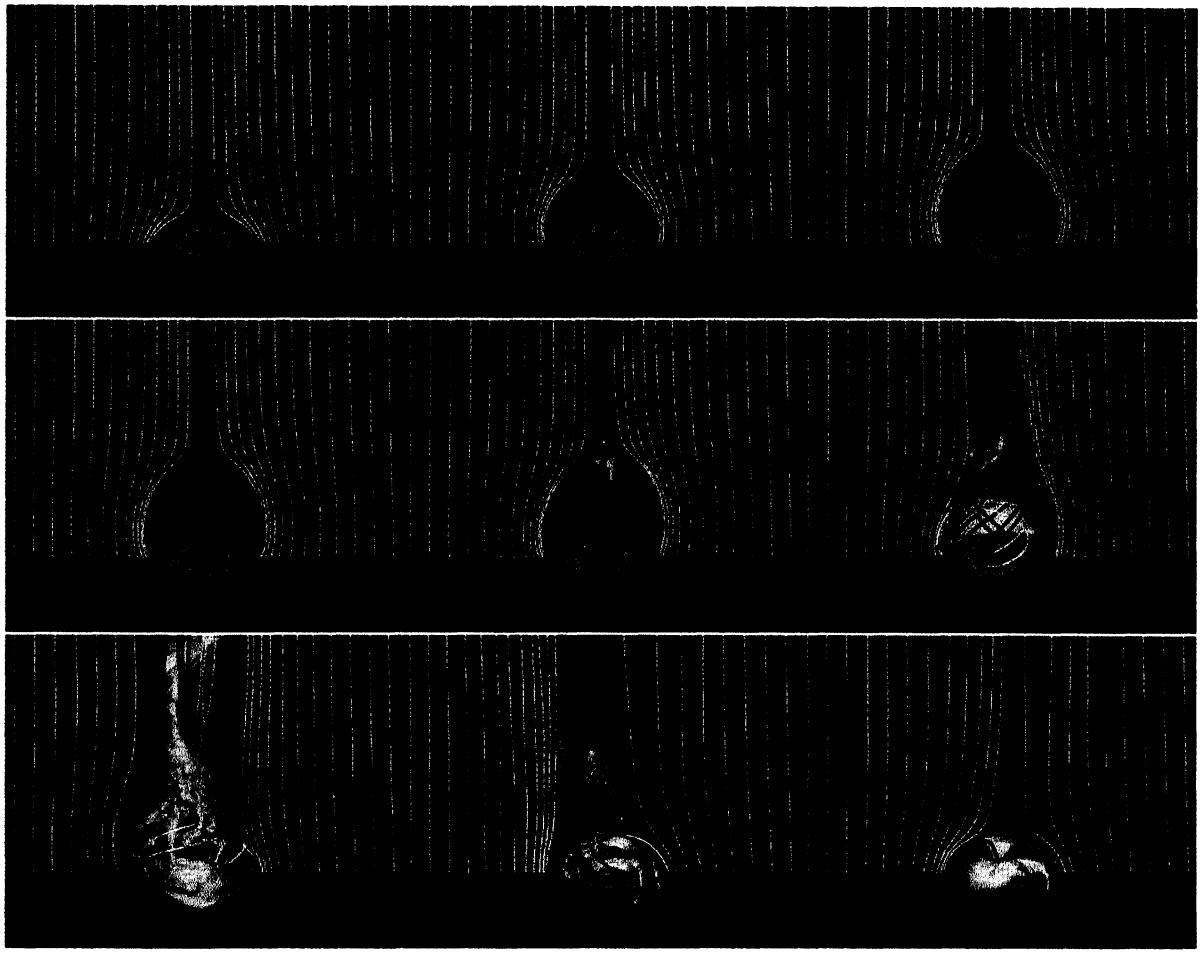

Fig. 4. Evolution of the magnetic configuration. The 2D horizontal plane displays the distribution of $|\mathbf{B}|$ at the bottom boundary (as in Fig. 1). The field lines are plotted starting from fixed position at the bottom boundary along the y axis. The white ones initially belong to the open connectivity domain whereas the blue ones are in the closed connectivity domain. The yellow isocontours correspond to mass density, $\rho = 1.25$.

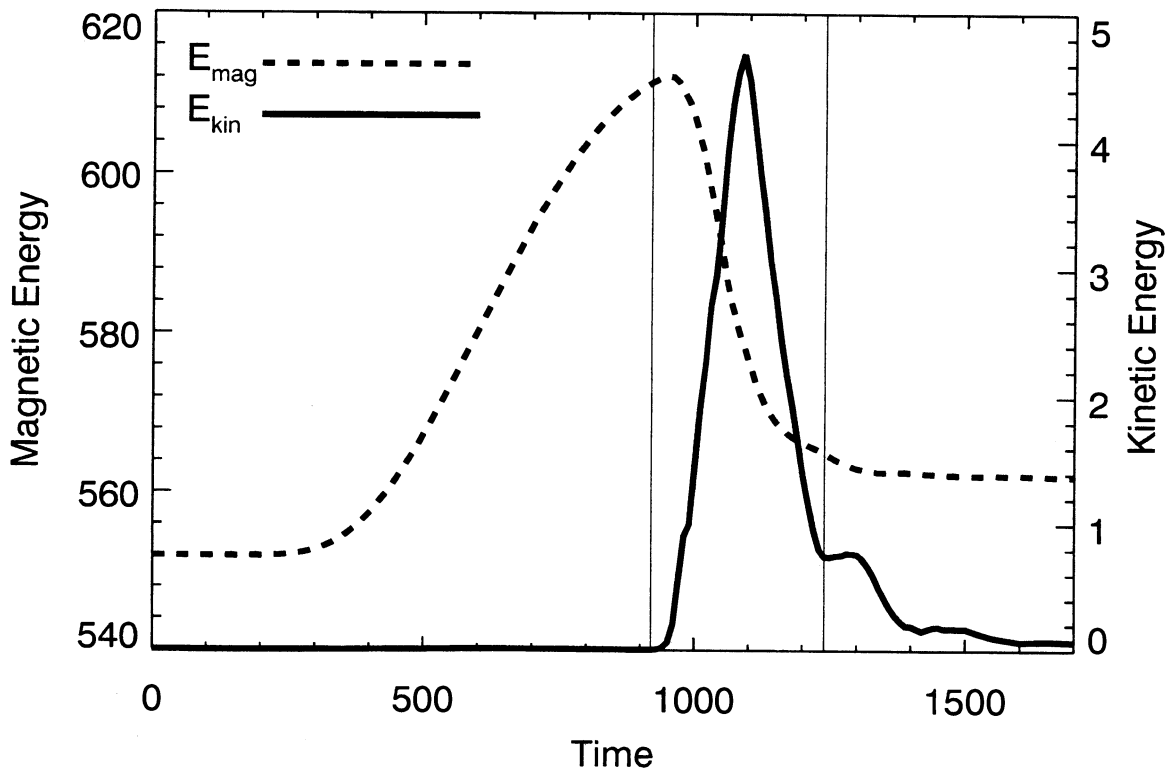

Fig. 5. Evolution of the kinetic (solid line) and the magnetic (dashed line) energies during the simulation. The two vertical lines at $t = 920$ and $t = 1240$ separate the three evolutionary phases.

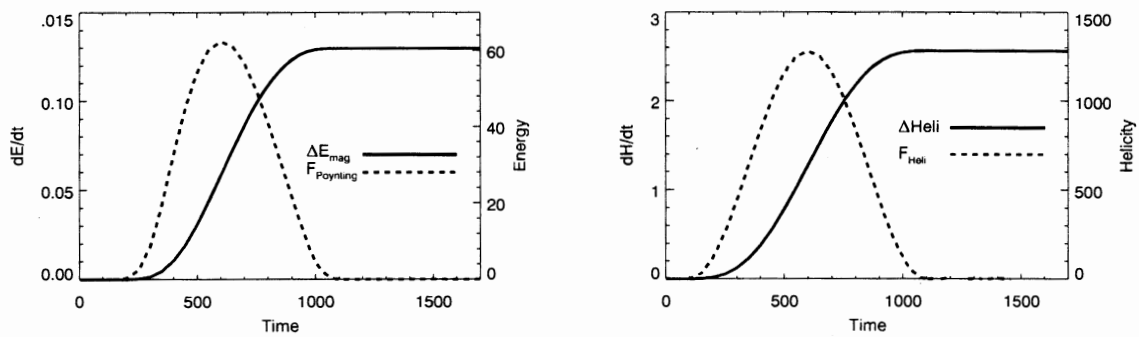

Fig. 6. Injection of energy and helicity through the bottom (photospheric) boundary ($z = 0$). **Left:** Poynting flux (dashed curve) and total magnetic energy injection (solid curve) estimated by integrating the Poynting flux. **Right:** Magnetic helicity flux (dashed curve) and total helicity (solid curve) estimated by integrating this flux .

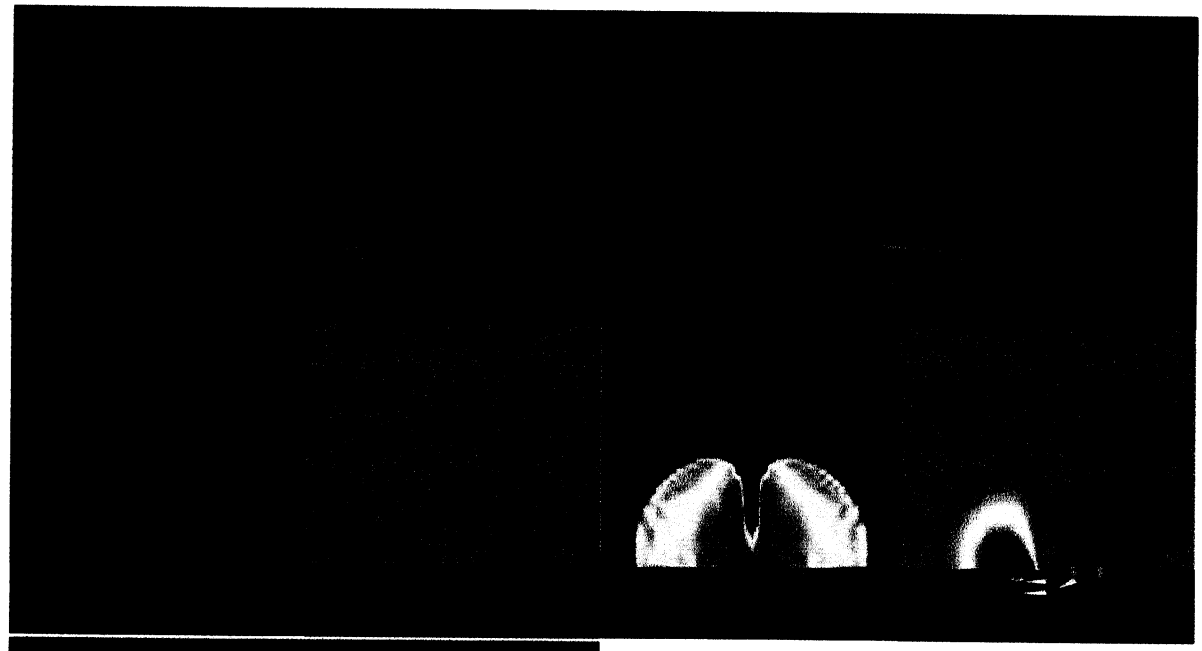

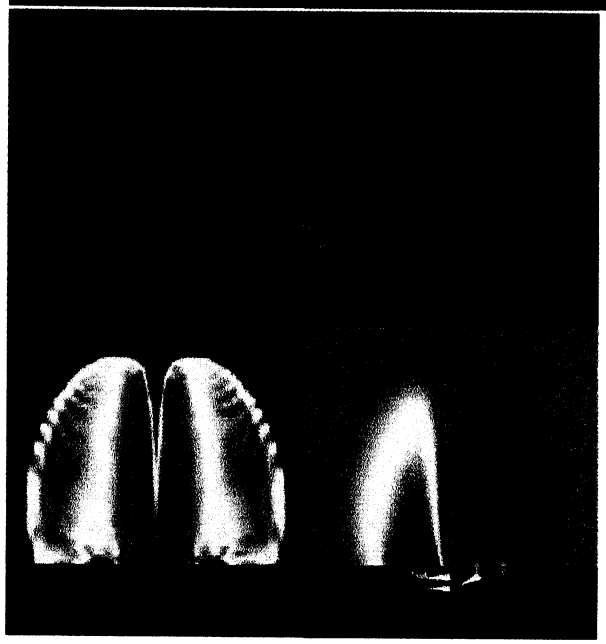

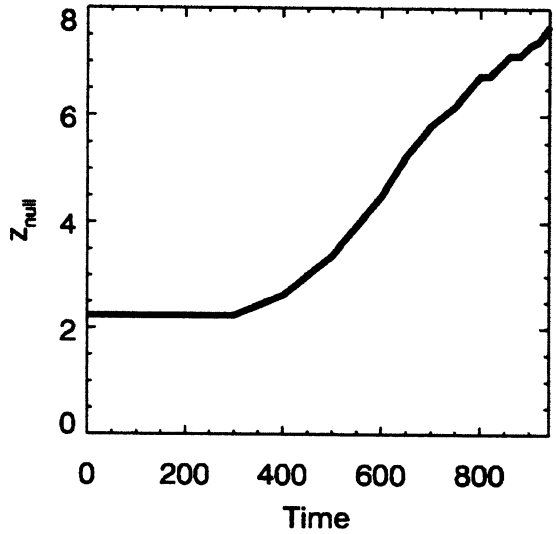
8
6
4
2
0
Z_{null}
0
200
400
600
800
Time

Fig. 7. Evolution of the magnetic configuration during the initial phase. **At each time: upper panel:** evolution of the inner fan (blue field lines) and the null point (red isosurface). The 2D filled contours on the bottom plane show the distribution of the magnetic field $|\mathbf{B}|$ at the bottom (photospheric) boundary (with a color shading similar to the one in Fig. 1). A green field line indicates the number of turns of the magnetic field within the inner polarity. **Bottom left:** vertical 2D distribution of the electric current $|\mathbf{j}|$ on the $y = 0$ plane. [purple; blue; cyan; green; yellow; red] correspond to current intensity of respectively [1; 0.8; 0.6; 0.4; 0.2; 0]. The lower horizontal slice displays the distribution of $|\mathbf{B}|$. **Bottom right:** vertical 2D distribution of the magnetic field component B_y on the (xz) plane at $y = 0$ (component perpendicular to the plane). [purple; blue; cyan; green; yellow; red] correspond to algebraic field intensity (positive indicated field toward the observer) of respectively [-4; -2.4; -0.8; 0.8; 2.4; 4]. The lower horizontal slice represent the distribution of $|\mathbf{v}|$. [purple; blue; cyan; green; yellow; red] correspond to velocity intensity of respectively [0.25; 0.2; 0.15; 0.1; 0.05; 0]. The arrows show the direction of the velocity field $\mathbf{v}$. **Bottom right panel:** evolution of the altitude of the null point during the simulation.

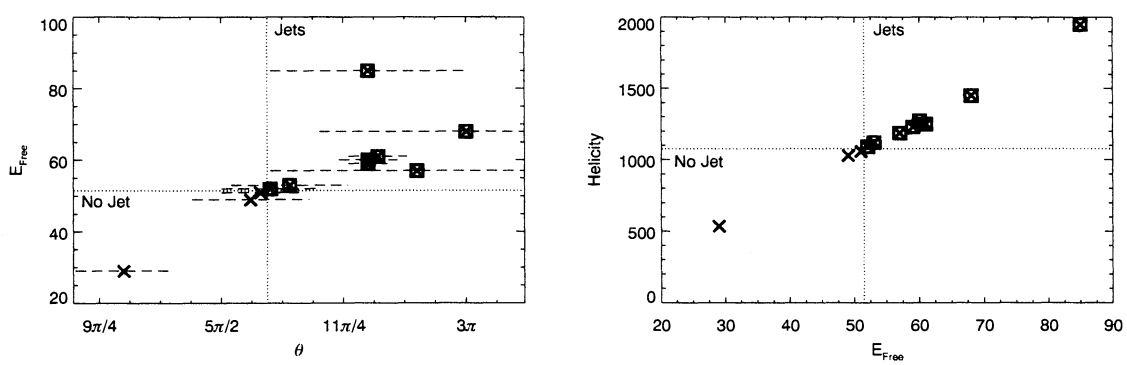

Fig. 8. Scatter plots of the twist angle θ, magnetic helicity, and free energy at the time of the instability or at the end of the simulation (if no instability occurred). The twist angle θ is the maximum angle of rotation of the field lines around the inner spine: $\theta{=}2\pi N_{turn}$. Each cross correspond to the result of a particular run. The boxed crosses correspond to runs in which an instability occurred. **Left:** free energy as a function of the twist angle θ. The dashed horizontal segments correspond to the margins of error. **Right:** helicity as a function of the free energy. The threshold values for an instability to occur are indicated by the dotted lines.

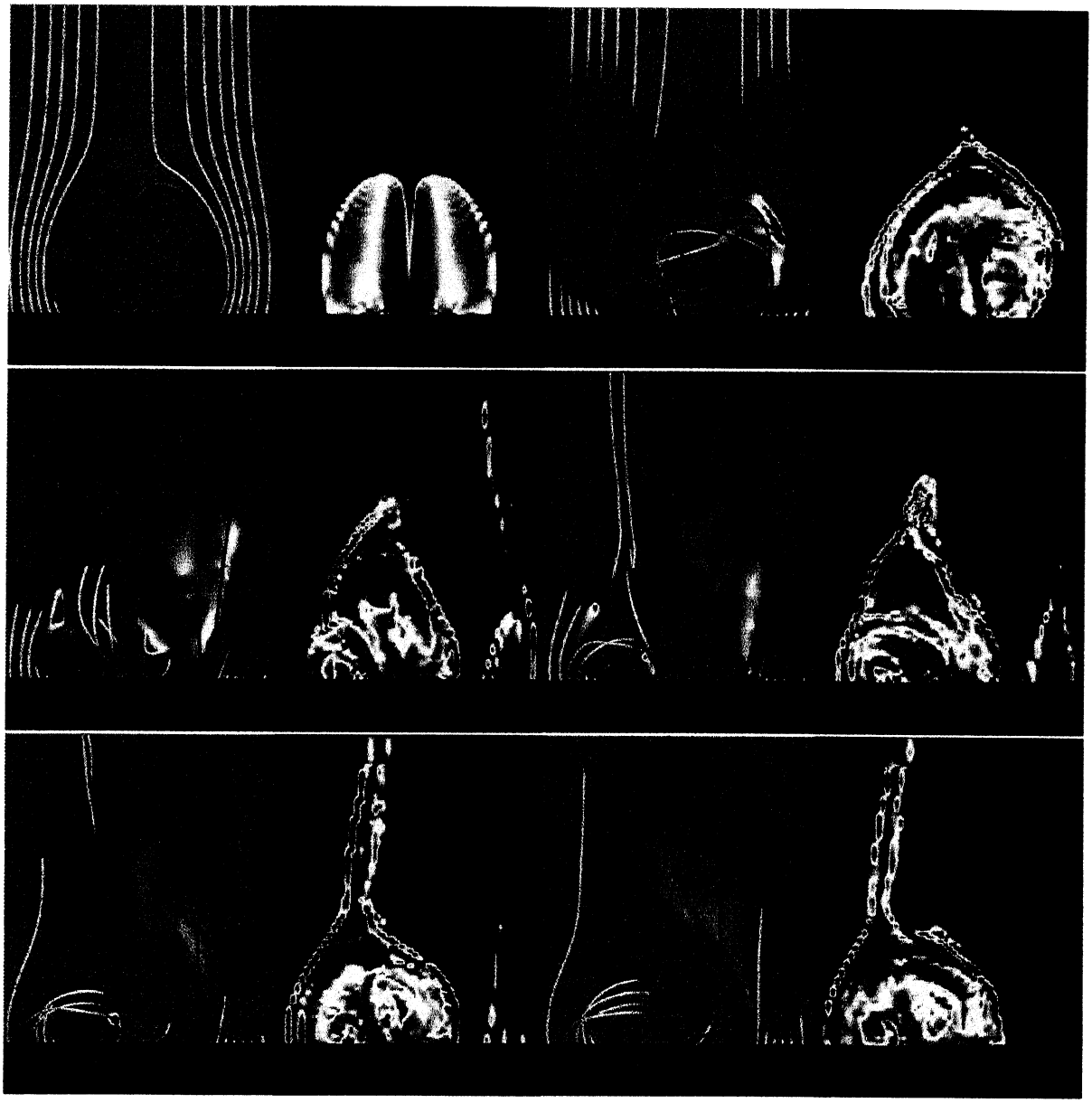

Fig. 9. **At each time: left:** vertical cut (in the (yz) plane at $x = 0$) of the vertical component v_z of the velocity field. [purple; blue; cyan; green; yellow; red] correspond to the algebraic v_z values (positive values for upflows) of respectively [0.28; 0.17; 0.06; −0.06; −0.17; −0.28]. The field lines are piloted starting from the bottom boundary along the y axis at fixed position: white field lines initially belongs to the open connectivity domain whereas the blue ones are in the close domain. **Right:** vertical cut (in the (yz) plane at $x = 0$) of the total current density. [purple; blue; cyan; green; yellow; red] correspond to current intensity of respectively [1; 0.8; 0.6; 0.4 ;0.2; 0]

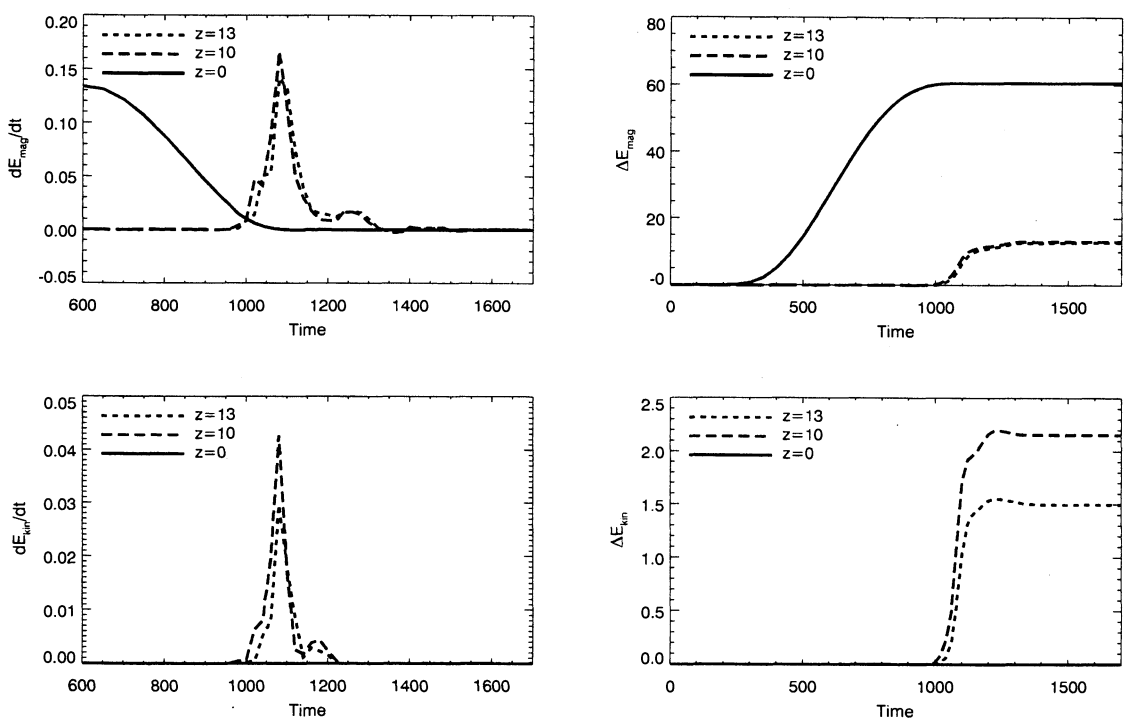

Fig. 10. Flux **(left column)** and time integrated variations **(right column)** of the magnetic energy **(top row)** and kinetic energy **(bottom row)** through horizontal (xy) planes at $z = 0$, 10, and 13.

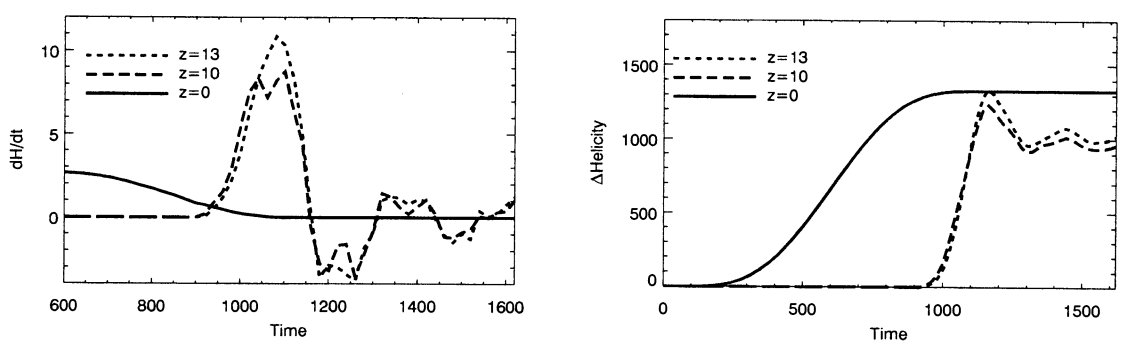

Fig. 11. Flux **(left)** and time integrated variations **(right)** of the magnetic helicity through horizontal (xy) planes at at $z = 0$, 10, and 13.

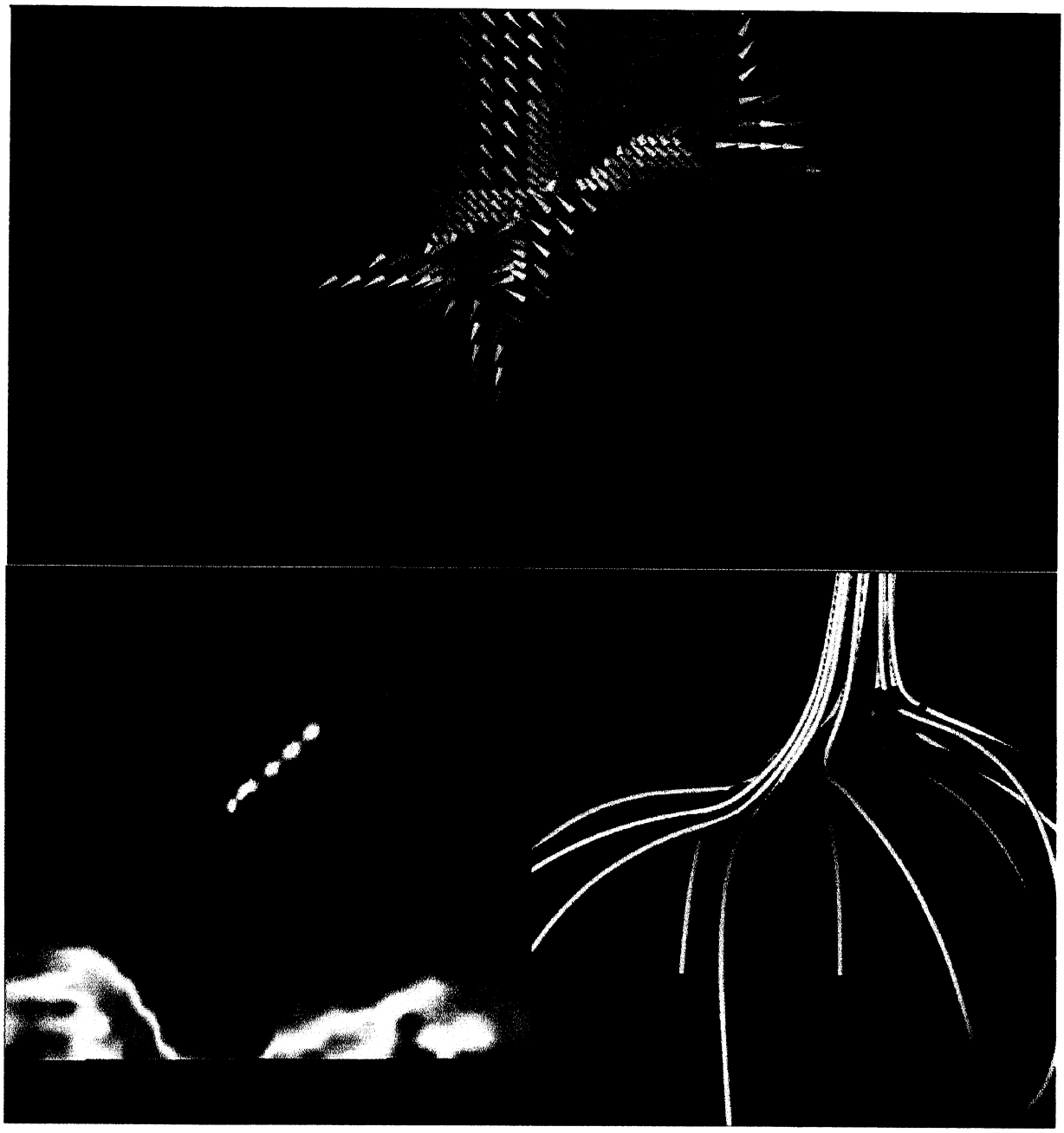

Fig. 12. Configuration at $t = 1360$. **Top:** vector velocity field in the (yz) plane $x = 0$. The color shading depends of the intensity of $|\mathbf{v}|$: [purple; blue; cyan; green; yellow; red] code respectively for [0.25; 0.2; 0.15; 0.1 ;0.05; 0]. **Bottom left:** distribution of the current density $\mathbf{j}$ in the (yz) plane at $x = 0$. **Bottom right:** magnetic field topology. The blue field lines locate the position of the inner spine and fan surface. The white field lines map the position of the outer spine and fan surface. The red isosurface delimits the volume of very low magnetic field ($|\mathbf{B}| < 0.2$). In each panel the bottom horizontal slice represents the distribution of the magnetic field $|\mathbf{B}|$ (with a color shading similar to the one in Fig. 1).